Materials Advances

ROYAL SOCIETY OF CHEMISTRY

PAPER

View Article Online
View Journal

Cite this: DOI: 10.1039/d5ma01288k

Structure–property relationships in chalcones with extended π-conjugation: ICT perturbation and red fluorescence

Brian Corbin, Paityn Houglan, Wei-Yuan Chen, Christopher J. Ziegler and Yi Pang *

4-Dimethylamino-2′-hydroxychalcone (**DHC**) derivatives are known to exhibit distinctive photophysical properties for various applications, including highly fluorescent crystals and molecular imaging. In a continuous effort to establish the structure–property correlation of this class of materials, a series of methoxy-substituted chalcone derivatives with extended π-conjugation have been synthesized to understand the effect of methoxy substituents on the intramolecular charge transfer (ICT) along the backbone. These derivatives displayed low fluorescence in protic solvents (*e.g.* $\phi_{fl} \approx 0.003–0.009$ in H_2O), but high fluorescence in a polar aprotic solvent ($\phi_{fl} \approx 0.2–0.35$ in DMSO), with emission maxima up to 658 nm. Fluorescence lifetime measurements revealed that the major emissive species could be attributed to locally excited (LE) and ICT states, while their emissive composition was heavily dependent on the methoxy-substitution pattern. The proposed predominant ICT mechanism was confirmed by low temperature fluorescence spectroscopy and supported by TDDFT calculations. Single crystal X-ray crystallography provided structural evidence for the chalcone derives, showing that the methoxy substituents could induce different tortional angles between the aromatic A-ring and the electron donor–acceptor backbone. The degree of the torsional angles was consistent with the number of the methoxy substituents present on the A-ring. These chalcone crystals were also highly fluorescent, with red-shifted emission (up to 703 nm) and quantum yield as high as Φ_{fl} = 0.363. This study explores a new class of chalcones that exhibit high fluorescence in both solution and solid states, and emission in the desirable red region.

Received 6th November 2025,
Accepted 16th March 2026

DOI: 10.1039/d5ma01288k

rsc.li/materials-advances

Introduction

Chalcones, or 1,3-diphenyl-2-propen-1-ones, are a class of naturally occurring bioactive compounds belonging to the flavonoid family and serve as synthetic precursors to flavonoids. Structurally, chalcones consist of two aryl rings (A and B) connected by an α,β-unsaturated carbonyl moiety (Fig. 1). Chalcones are naturally nontoxic and are found in a variety of fruits, vegetables, roots, and seeds.[1] Naturally occurring chalcones exhibit a broad range of biological activities, including antioxidant, anticancer, anti-inflammatory, antidiabetic, and antibacterial properties.[2–8] The low toxicity and therapeutic benefits of many natural chalcones have made them promising candidates for use as therapeutic sensing applications.

In addition to their favorable biological activities, chalcones also display attractive optical properties. For instance, crystals of 4-dimethylamino-2′-hydroxychalcone (**DHC**) are among the most fluorescent organic crystals reported.[9] Another interesting chalcone derivative is **2DHC**, in which the vinylene linkage is extended to include the –(CH═CH–CH═CH)– linkage. Although **2DHC** exhibits desirable red emission (λ_{em} at 676 nm in MeOH), it remains weakly fluorescent in solution.[10] Both hydroxychalcones, **DHC** and **2DHC**, display

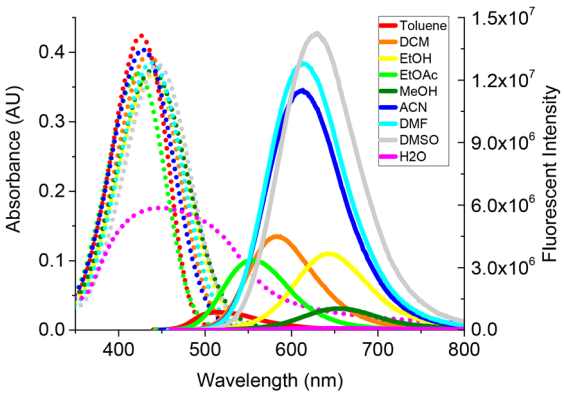

Fig. 1 Absorbance (dotted lines) and emission (solid lines) of chalcone **1a** in various organic solvents. Dye concentration of 10 μM.

Department of Chemistry, The University of Akron, Akron, OH, 44325, USA.
E-mail: yp5@uakron.edu

large Stokes shifts, an attractive feature for sensing applications. This characteristic is attributed to the presence of a 2′-hydroxy group capable of undergoing excited-state intramolecular proton transfer (ESIPT). To advance the use of chalcones in optoelectronic materials and molecular imaging, it is critical to elucidate the structure–property relationships that govern their fluorescence, with the aim of enhancing their emission properties.

Few molecular probes incorporating **DHC** scaffolds have been reported, in part due to their inherently low fluorescence in solution. Notable examples include **DHC** derivatives developed for albumin detection,[11,12] Al^{3+} sensing in live cells,[13] and a fluoro-PEG-substituted DHC employed for *in vivo* imaging of Aβ aggregates and plaques associated with Alzheimer's disease.[14] In contrast, even fewer sensors have been developed using the **2DHC** framework, despite its ability to emit in the red to near-infrared (NIR) region—a desirable property for therapeutic sensing due to reduced background autofluorescence and improved tissue penetration, which together enable clearer imaging of thick biological samples.[15,16] For example, **2DHC** displays absorption and emission maxima at 455 and 676 nm, respectively, in methanol. However, the parent **2DHC** scaffold exhibits poor fluorescence quantum yields in solution, which limits its broader application in the development of fluorescent sensors for molecular imaging.[17,18]

Fluorophores exhibiting large Stokes shifts are particularly desirable for optical sensing and imaging applications, as they minimize self-absorption and excitation–emission crosstalk while suppressing background interference from scattered excitation light.[19–21] These attributes lead to improved signal-to-noise ratios and more reliable detection, especially in complex or highly scattering environments such as biological media and solid-state matrices.[22] In addition, large Stokes shifts provide greater flexibility in optical filter selection and facilitate multiplexed detection by reducing spectral overlap among different emitters. From a molecular design perspective, large Stokes shifts often originate from substantial excited-state reorganization, including intramolecular charge transfer (ICT), making them a useful photophysical signature for evaluating donor–acceptor coupling and excited-state relaxation pathways.[23,24] Accordingly, fluorophores that combine red emission with large Stokes shifts represent attractive platforms for the development of advanced optical probes.

In our previous report, low-temperature fluorescence measurements revealed that the long-wavelength emission of **2DHC** arises from a combination of intramolecular charge transfer (ICT) and ESIPT processes.[10] To further elucidate the photophysical behavior of this class of compounds, we synthesized a series of chalcone derivatives, **1a–f**, in which the ESIPT pathway is eliminated to isolate and examine the influence of ICT on fluorescence. Although **1a** has previously been reported to exhibit low fluorescence quantum yields in various solvents,[25,26] our study focuses on tuning ICT efficiency through strategic alkoxy substitution at different positions on the aromatic ring. This investigation includes solvent-dependent emission analysis, low-temperature (77 K) fluorescence spectroscopy, solid-state emission studies, single-crystal X-ray diffraction, and computational analysis to compare theoretical and experimental results. Notably, several derivatives within this series exhibited markedly enhanced fluorescence in comparison with **2DHC**; for instance, **1c** displays a quantum yield of $\Phi_{fl} \approx 0.3$ in DMSO and $\Phi_{fl} \approx 0.04$ in MeOH. Furthermore, despite the absence of ESIPT, the emission of **1a** derivatives remains in the desirable red/far-red region (600–700 nm), highlighting their potential utility in biological imaging and optoelectronic applications (Scheme 1).

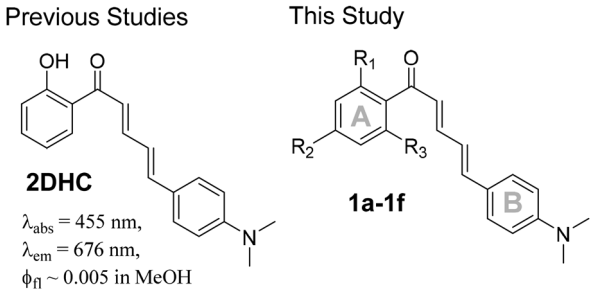

Scheme 1 Chemical structures of chalcones **2DHC** and **1a**.

Materials and methods

General synthesis

Chalcones **1a–1f** were synthesized *via* a pyrrolidine catalyzed Knoevenagel condensation between the appropriate acetophenone derivatives **2a–2f** and 4-(dimethylamino)cinnamaldehyde. In general, the acetophenone derivative (1.1 mmol) and 4-(dimethylamino)cinnamaldehyde (1.0 mmol) were combined in ethanol (5 mL) in a 50 mL round-bottom flask and stirred for 5 min to ensure complete dissolution. Pyrrolidine (0.10 mL) was then added dropwise, and the reaction mixture was stirred at room temperature for 18 h. Upon completion, the reaction mixture was poured into ice-water (120 mL) and adjusted to pH ~ 6. The resulting mixture was extracted with dichloromethane (3 × 30 mL), and the combined organic layers were concentrated under reduced pressure. The crude products were purified by column chromatography on silica gel using dichloromethane as the eluent to afford chalcones **1a–1f** in good yields. Detailed experimental procedures and characterization data for each derivative are provided in the SI.

Compounds **2a–2f** and **3** for synthesis were purchased from Sigma Aldrich or Fischer Scientific and were used without further purification. UV-vis spectroscopy was performed using a Hewlett Packard-8453 diode array spectrophotometer at 25 °C. Excitation and fluorescence spectra were measured using a HORIBA Fluoromax-4 spectrofluorometer. ^{1}H NMR spectra were obtained on a Varian 500 MHz spectrometer in deuterated chloroform ($CDCl_3$).

Mass spectrometry analysis was performed using a Bruker timsTOF Pro 2 Q/ToF, equipped with an electrospray ionization (ESI) source. Mass calibration was conducted by using ESI-L low concentration tuning mix (Tune Mix) from Agilent Technologies (Santa Clara, CA). All mass spectral data were collected using timsControl (Billerica, MA) and analyzed using Compass DataAnalysis (Billerica, MA) software.

Single crystal X-ray diffraction studies were performed using a Bruker PHOTON II CPAD-based diffractometer with dual Cu/Mo ImuS microfocus optics. The detector was placed at 5.00 cm from the crystal, and the data were corrected for absorption with the SADABS program. The structures were refined using the Bruker SHELXTL Software Package (Version 6.1) and were solved using direct methods until the final anisotropic full-matrix, least squares refinement of F2 converged. Single crystals suitable for X-ray diffraction were obtained by vapor diffusion (chloroform/pentane) or slow evaporation from ethyl acetate.

Absolute fluorescence quantum yields were collected on a Jobin Yvon Horiba Fluoromax-4 using a calibrated Horiba integrating sphere #5570830005. Absorbance intensity was maintained below 0.1.

Low temperature fluorescence spectra were recorded by dissolving the probe in ethanol (10 μM). The ethanolic solution was transferred to a quartz tube and then quickly submerged into a quartz dewar filled with liquid nitrogen. Once frozen, the dewar was placed into the instrument and optical properties were measured.

Results and discussion

Photophysical properties in solution

In the study, **1a** was used as a reference compound, whose structure involves donor–acceptor (D–A) interaction. It was noticed that the absorption remained relatively unchanged in a wide range of solvents used, with $\lambda_{abs} \approx 420$–$445$ nm (Fig. 1). However, the fluorescence of **1a** revealed a significant positive solvatochromic effect, with emission peaks at 518 nm (in toluene) and 658 nm (in EtOH), which is characteristic of ICT fluorophores. This sensitivity arises from the large excited-state dipole moment, which is stabilized by polar solvents, resulting in enhanced fluorescence and red-shifted emission.

After establishing the optical properties for model chalcone **1a**, our attention turned to examination of derivatives **1b–1f**, to establish a structure–property relationship between substituent positioning and the corresponding optical response. We hypothesized that the fluorescence properties of **1a** could be affected by placing a methoxy substituent on the *ortho*- and/or *para*-positions of the A-ring, since these positions could exert an electronic effect directly influencing the existing intramolecular charge transfer (ICT) that involves the carbonyl group in **1a**. Thus, derivatives **1b** and **1c** were synthesized by introducing a single –OMe group on the A-ring. As shown in Table 1, the methoxy group caused a slight hypsochromic shift in both absorption λ_{abs} (by ~6–13 nm) and fluorescence λ_{em} (9–15 nm from **1a**) in DMSO. A plot of fluorescence λ_{em} *versus* solvent dielectric constant (Fig. 2a) revealed a significant positive solvatochromic effect.

These results indicated that the –OMe substituent perturbed the major ICT interaction between the $-NMe_2$ and C═O groups (Fig. 2b). A detailed analysis of the electron density redistribution upon excitation, obtained from computational modelling, is presented in the Theory section. In Fig. 2a, the solvents are listed in order of increasing dielectric constant: toluene (Tol) < EtOAc < CH_2Cl_2 (DCM) < EtOH < MeOH < acetonitrile (CH_3CN) < dimethyl sulfoxide (DMSO) < H_2O.

In derivatives **1d** and **1e**, two –OMe groups were present on the A-ring at the respective 2′,4′- and 2′,6′-positions. Compound **1d** showed a λ_{abs} (*e.g.*, 433 nm in DMSO) nearly identical to that of mono substituted **1b** (Table 1 and S13, SI). In contrast, **1e** exhibited an additional hypsochromic shift in λ_{abs} (*e.g.*, 421 nm in DMSO), suggesting that the *para*-substituent plays a less significant role. Interestingly, the spectral difference between **1d** and **1e** became more pronounced in their fluorescence ($\Delta\lambda_{em} \approx 37$ nm; Fig. 2a). It appears that two –OMe groups at the *ortho*-positions introduce a synergistic effect—likely *via* steric hindrance—causing a substantial blue-shift in emission. This was further confirmed by observing similar emission from the tri-substituted derivative **1f** (Fig. 2a). The emission wavelength λ_{em} followed the trend **1a** > **1b** > **1c** > **1d** > **1e** > **1f**, consistent with increasing steric hindrance on the A-ring.

The chalcone molecule **1** in its ground state is expected to exist in a neutral form. Based on ^{1}H NMR and X-ray structural analysis, both vinyl bonds adopt the *trans*-configuration. Upon

Table 1 The synthesis and optical properties of **1a–1f**

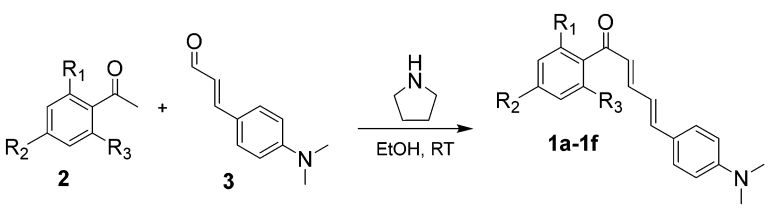

Compound	R_1	R_2	R_3	λ_{abs} (nm)[a]	λ_{em} (nm)[a]	$\Delta\lambda$ (cm^{-1})[a]	ε (M^{-1} cm^{-1})[a]	Φ_{fl}[a]
1a	H	H	H	446	630	6549	38 200	0.350
1b	OMe	H	H	433	621	6992	44 000	0.283
1c	H	OMe	H	440	615	6467	53 800	0.301
1d	OMe	OMe	H	433	607	6620	45 100	0.245
1e	OMe	H	OMe	421	570	6209	39 900	0.053
1f	OMe	OMe	OMe	420	568	6204	41 000	0.048

[a] Optical properties recorded in DMSO.

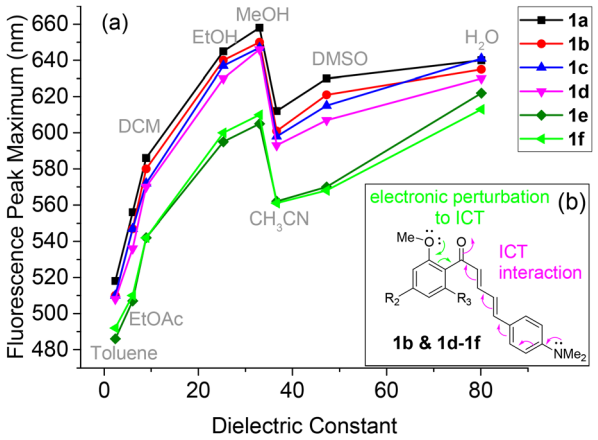

Fig. 2 (a) Plot of fluorescence λ_{em} *versus* solvent dielectric constant for **1a–1f**. (b) The inset shows the electronic perturbation of the ICT interaction.

photon absorption, the electron density shifts from the donor (D) to the acceptor (A) group *via* ICT, producing a zwitterionic form (Fig. 3a). Since **1a** supports a greater extent of ICT, its emission occurs at a longer wavelength. When one –OMe group is present on the A-ring, as in **1b**, the lone-pair of electrons on the methoxy group can interact with the carbonyl group, perturbing or weakening the ICT process (Fig. 2b) and causing a hypsochromic shift in emission. Two –OMe groups are expected to further increase electronic perturbation, producing an additional hypsochromic shift. Because steric interaction alone cannot explain why **1b** exhibits a longer-wavelength emission than **1c** (which has lower steric demand), an electronic contribution must be invoked. Notably, the *para*-substituted –OMe group in **1c** exhibits minimal steric interaction with the carbonyl group, allowing the aromatic A-ring to achieve better conjugation with the C═O group, thereby enabling a stronger perturbation and a larger hypsochromic shift.

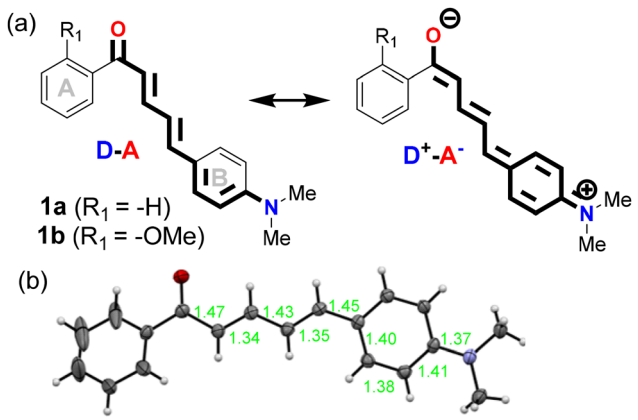

Fig. 3 (a) Chalcones 1 in its neutral (D–A) and zwitterionic (D^+–A^-) forms. The polymethine chain connecting donor (D) and acceptor (A) is expressed in darker lines for clarity. (b) The molecular structure of **1a** with 35% thermal ellipsoids from X-ray crystallography analysis, showing the bond lengths (in Å) along the polymethine chain.

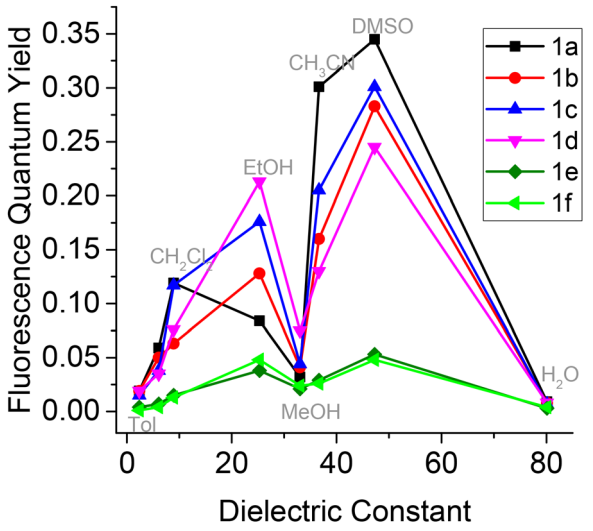

Fig. 4 Dependence of the experimental fluorescence quantum yield (Φ_{fl}) on the dielectric constant of the solvent.

In addition to the impact on wavelengths, the fluorescence quantum yields (Φ_{fl}) of **1a–1f** were also evaluated in various solvents (Fig. 4). Derivatives **1e** and **1f** displayed lower Φ_{fl} values than **1a–1d**, especially in polar aprotic solvents such as DMSO, showing the influence of substitution pattern on quantum yield.

Overall, the number and position of –OMe groups in **1b–1f** caused hypsochromic shifts in both absorbance and emission, and reduced the quantum yields. When the A-ring exhibits greater rotational freedom, the optical performance improves—for example, **1d** displays better properties than **1e**, as the 6′-methoxy group in **1e** imposes greater steric hindrance than the 4′-methoxy group in **1d**. The steric interactions of 2′- and 6′-methoxy groups in **1e** and **1f** may promote *cis–trans* isomerization in the excited state, accounting for their sharp decreases in quantum yield and pronounced hypsochromic shifts relative to monosubstituted derivatives. The sterically hindered **1f**, bearing methoxy groups at the 2′, 4′, and 6′ positions, produced the largest hypsochromic shifts and a nearly 7.3-fold reduction in quantum yield, from 0.35 for **1a** to 0.048 in DMSO. These observations agree with literature reports that sterically induced TICT geometries in donor–acceptor chromophores lead to diminished radiative efficiency and large emission blue-shifts under polar solvent conditions.[27–30]

To directly probe the role of intramolecular motion in excited-state deactivation, viscosity-dependent fluorescence measurements were performed in methanol/glycerol mixtures (Fig. S20). Increasing viscosity led to systematic fluorescence enhancement for all derivatives, while absorption profiles remained largely unchanged, consistent with suppression of motion-induced nonradiative decay. In 90% glycerol/MeOH, the fluorescence quantum yields of the methoxy-substituted derivatives converge to similar values (Φ_{fl} = 0.202–0.235), slightly exceeding that of the unsubstituted reference **1a** (Φ_{fl} = 0.146) (Table S2). Notably, the sterically congested *ortho*-substituted derivatives **1e** and **1f**, which exhibit low Φ_{fl} in

low-viscosity solvents, now display quantum yields comparable to those of **1b–1d**. This behavior is consistent with the viscous environment suppressing sterically facilitated torsional relaxation and excited-state *cis–trans* isomerization along the enone/diene backbone, processes that dominate nonradiative decay for these derivatives in fluid solution. These results indicate that viscosity restricts A-ring-backbone motion and limits structural relaxation pathways that are readily accessible under low-viscosity conditions.

Low temperature spectroscopy

To further probe the excited-state relaxation behavior of the synthesized chalcone derivatives, low-temperature excitation and fluorescence measurements were performed by freezing the molecules in ethanol. Solutions were frozen in liquid nitrogen (−189 °C), effectively immobilizing the molecular framework and suppressing large-amplitude motions such as torsional relaxation, *cis–trans* isomerization, and solvent reorganization that normally accompany intramolecular charge-transfer relaxation at room temperature.

Compounds **1a** and **1e** have low and high rotational barriers along the bond between the A-ring and carbonyl group, which lead to their large difference in λ_{em} (Table 1). Upon cooling to −189 °C, the fluorescence spectra of chalcone **1a** were shifted drastically by ∼90 nm to λ_{em} = 555 nm, from λ_{em} = 645 nm at 20 °C (Fig. 5a). Under the same conditions, fluorescence of **1e** at −189 °C also revealed a similar pattern, showing a large spectral blue shift by ∼54 nm to λ_{em} = 541 nm, from λ_{em} = 595 nm at 20 °C (Fig. 5b). In the frozen matrix, the fluorophores were unable to adopt the fully relaxed ICT geometry that led to emission from a higher-energy excited-state configuration, giving rise to the blue-shifted emission and enhanced fluorescence due to the reduction of nonradiative decay pathways.

It was assumed that the molecular structure observed at −189 °C would resemble that of the locally excited (LE) state, as torsional motions are frozen under these conditions. In other words, the fluorescence detected at −189 °C came from an excited state that had not undergone ICT. By contrast, fluorescence observed at room temperature reflected states that had relaxed through ICT. Based on the large spectral shift between room- and low-temperature fluorescence, it was assumed that **1a** permitted a greater extent of ICT than **1e**. This conclusion is consistent with the experimental observation that **1a** emits at a longer wavelength than **1e** at room temperature, reflecting stronger ICT stabilization. The result was consistent with the assumption that substantial geometry changed during the LE → ICT relaxation pathway.

The spectra of the frozen **1a** also revealed partially resolved structures, showing vibronic bands in both excitation and emission spectra (Fig. 5a). The structured emission peaks at 508 and 555 nm corresponded to 19 685 cm^{-1} and 18 018 cm^{-1}, respectively. Based on the spectral overlap with excitation, the emission peak at 508 nm was assumed to be a 0–0 transition, and 555 nm to be a 0–1 transition. Similarly, the low temperature emission peaks of **1e** at 489 nm (= 20 449 cm^{-1}) and

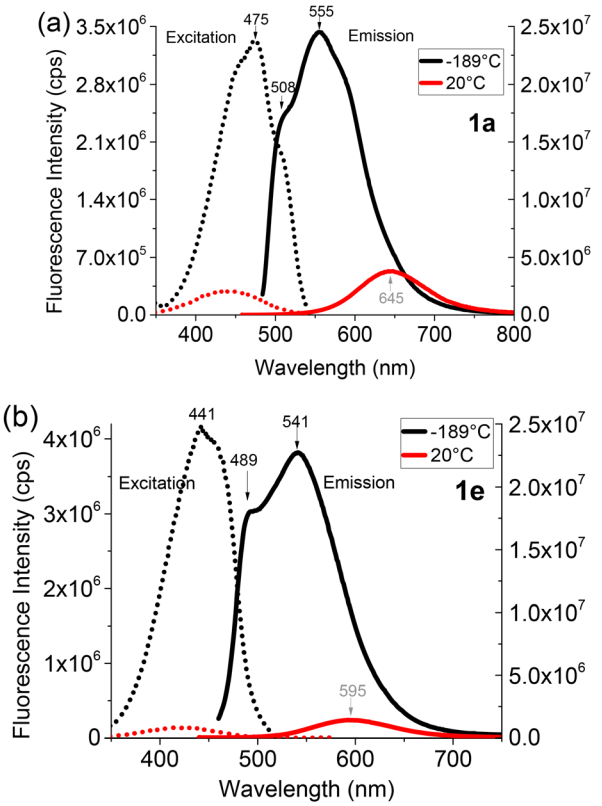

Fig. 5 Low temperature excitation (dotted lines) and emission spectra (solid lines) of chalcones **1a** (a) and **1e** (b) in EtOH.

541 nm (= 18 484 cm^{-1}) could be assigned to 0–0 and 0–1 transitions, respectively.

Fluorescent lifetime

Time-resolved fluorescence measurements in acetonitrile (Table 2) and other solvents (Table S3, SI) revealed biexponential decay kinetics for all chalcone derivatives, comprising a short-lived component (τ_1) assigned to emission from the locally excited (LE) state and a longer-lived component (τ_2) attributed to the emissive intramolecular charge transfer (ICT) state. Amplitude-weighted lifetimes ($\bar{\tau}$) were calculated according to:

$$\bar{\tau} = \frac{\sum(\alpha_i \tau_i)}{\sum \alpha_i}$$

where α_i and τ_i represent the fractional amplitudes and lifetimes of each component, respectively. In acetonitrile, the high-fluorescence derivatives **1a–1d** exhibit $\bar{\tau}$ values in the range of

Table 2 Fluorescent lifetimes of synthesized chalcone derivatives in acetonitrile

Compound	τ_1 (ns)	α_1 (%)	τ_2 (ns)	α_2 (%)	X^2	$\bar{\tau}$ (ns)	Φ_{fl}	k_r (ns^{-1})	k_{nr} (ns^{-1})
1a	0.69	10	1.285	90	1.21	1.23	0.301	0.245	0.53
1b	0.207	7	1.091	93	1.04	1.03	0.16	0.155	0.845
1c	0.504	9	0.913	91	1.11	0.879	0.205	0.233	0.795
1d	0.438	15	0.801	85	1.22	0.752	0.13	0.173	1.155
1e	0.17	95	0.6	5	0.89	0.191	0.029	0.152	5.026
1f	0.15	83	0.32	17	1.07	0.18	0.026	0.144	5.023

~0.75–1.23 ns (Table 2), with the decay dominated (≈85–93%) by the ICT component (τ_2 ≈ 0.80–1.29 ns). In contrast, the sterically congested *ortho*-methoxy derivatives **1e** and **1f** show substantially reduced $\bar{\tau}$ values (~0.18–0.19 ns), with the LE component comprising 80–95% of the decay. This inversion in amplitude weighting directly indicates suppression of ICT in these systems, consistent with sterically induced twisting due to the dual *ortho* substitution that electronically decouples the donor and acceptor segments. Similar lifetimes and amplitude distributions have been reported in related donor–acceptor systems.[18,31,32] In summary, the majority of the emission from **1a–1d** was from the ICT state. In contrast, the emission from **1e** and **1f** was mainly from the LE state (Table 2). The assumption could be explained by considering the stability of the excited ICT state, as the steric interaction between the vinyl proton and –OMe group destabilizes the ICT state for **1e** and **1f** (structure in Table 1).

Radiative (k_r) and nonradiative (k_{nr}) rate constants were determined directly from the ACN lifetimes and quantum yields (Φ_{fl}) according to:

$$k_r = \frac{\Phi_{fl}}{\bar{\tau}}$$

$$k_{nr} = \frac{(1 - \Phi_{fl})}{\bar{\tau}}$$

Radiative rates were similar across the series (~0.14–0.34 ns^{-1}), indicating that intrinsic emission probability is largely insensitive to substitution pattern. In contrast, k_{nr} increased from 0.53–1.15 ns^{-1} for **1a–1d** to ~5 ns^{-1} for **1e–1f**, representing a ~5–10-fold acceleration of nonradiative decay in the *ortho*-substituted derivatives. This dramatic increase in k_{nr} is consistent with ultrafast intramolecular torsion or excited-state *cis–trans* isomerization as the dominant deactivation pathway. The strong enhancement in fluorescence quantum yield observed earlier for **1e** and **1f** upon freezing in ethanol at −189 °C further supports the role of large-amplitude motions in driving the observed quenching.

Crystal structures and solid-state optical properties

Solid-state excitation and emission properties were recorded (Fig. 6) and are summarized in Table 3. The series of compounds exhibited red/far-red emission with large Stokes shifts, and their emission maxima were in the order: **1f** → **1e** → **1b** → **1c** → **1d** → **1a**.

Single-crystal X-ray diffraction studies revealed distinct packing motifs across the chalcone series (Fig. 7), which strongly influence their solid-state photophysical properties. The most planar derivative, **1a** (A-ring torsion ≈ 21°, Fig. S22 and Table S4, SI), adopts a slip-stacked herringbone arrangement of the B-rings in a J-aggregate-like configuration (Fig. 8 and Fig. S23), with centroid distances of ~3.72 Å. This geometry enhances donor–π–acceptor conjugation and stabilizes the lowest exciton, accounting for the NIR crystalline emission (λ_{em} = 703 nm, Table 3). Consistently, the solid-state excitation spectrum of **1a** retains partially resolved vibronic peaks (Fig. 6), reflecting strong Franck–Condon coupling to a dominant

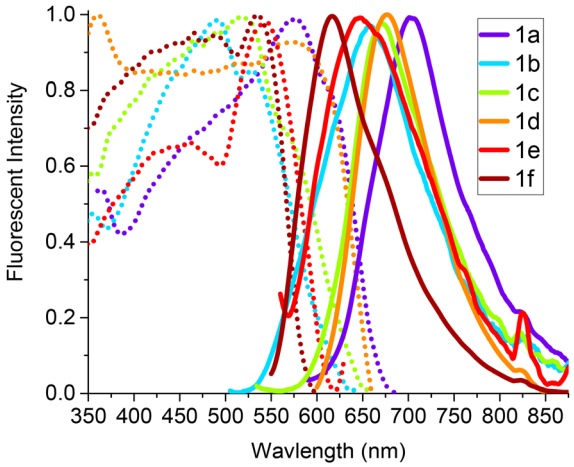

Fig. 6 Normalized solid-state excitation (dotted) and emission (solid) spectra of **1a–1f**.

Table 3 Solid state optical properties of **1a–1f**

Compound	λ_{ex} (nm)	λ_{em} (nm)	$\Delta\lambda$	Φ_{fl}
1a	575	703	128	0.332
1b	490	660	170	0.073
1c	522	673	151	0.212
1d	580	680	100	0.155
1e	545	650	105	0.030
1f	535	618	83	0.363

stretching mode. This behavior parallels the low-temperature spectra (Fig. 5a), where distinct 0–0 and 0–1 bands were observed, confirming that rigid slip-stacked packing suppresses torsional relaxation and preserves vibronic structure in the crystalline state.

In contrast, derivatives with larger torsional angles show progressive hypsochromic emission and less defined excitation features. **1b–1d** (torsional angle ~21–44°) emit in the 660–680 nm range, intermediate between **1a** and sterically hindered **1f**. For example, **1b** crystallizes in an ordered yet loosely coupled lattice with minimal face-to-face π-stacking of either ring system; adjacent A rings are twisted and laterally offset within extended lamellar domains (Fig. S24). This arrangement suppresses J-type coupling and leaves the 0–0 transition oscillator weak while failing to rigidify torsional motion, thereby facilitating nonradiative decay (k_{nr}) consistent with its low Φ_{fl}.

Interestingly, **1c** exhibits red-shifted absorption ($\Delta\lambda_{abs}$ = 32 nm), red-shifted emission ($\Delta\lambda_{em}$ = 13 nm), and a solid-state quantum yield (Φ_{fl} = 0.212) nearly three times higher than that of **1b**, despite both derivatives bearing a single methoxy substituent on the A-ring. This distinction is not observed in solution, where the two isomers display very similar photophysical properties, indicating that the divergence arises from differences in solid-state organization rather than intrinsic electronic effects. Structurally, **1c** adopts a substantially smaller A-ring–enone torsional angle (22.14°) than **1b** (43.52°), closely matching that of the planar reference compound **1a** (~21°). This reduced torsion preserves effective conjugation and

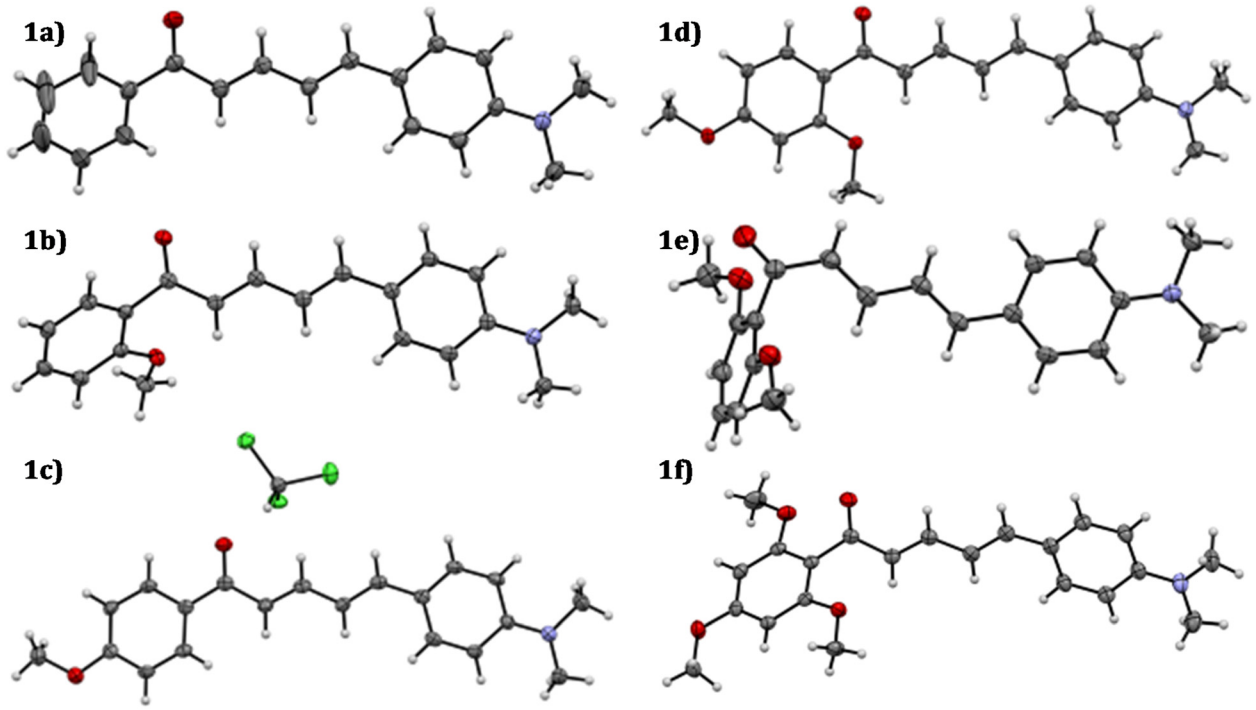

Fig. 7 Structures of chalcone derivatives **1a–1f** with 35% thermal ellipsoids.

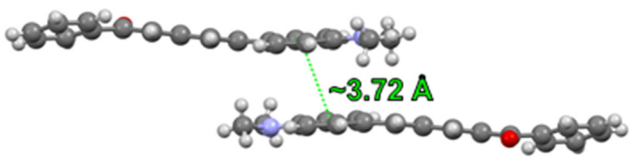

Fig. 8 Crystal packing of **1a**, showing the tendency to form a J-type interaction.

promotes well-defined molecular planes in the crystal lattice, despite a modest curvature of the chromophore backbone introduced by the extended diene bridge (Fig. S24 and S25). In contrast, the larger twist in **1b** disrupts planarity and limits intermolecular coherence in the solid state.

In the crystal, **1c** assembles into an edge-to-face, herringbone-like packing arrangement rather than forming extended cofacial π-stacked assemblies. A well-organized, co-crystallized chloroform molecule inserts between adjacent chromophores and engages in a directional C–H···O interaction with the carbonyl unit (≈2.18 Å), influencing lattice organization and suppressing the formation of J-aggregate-like stacks (Fig. S24 and S25). This packing motif limits strong intermolecular π–π interactions and moderates excitonic coupling while maintaining lattice rigidity. The combined effects of reduced torsional distortion, controlled backbone curvature, and suppressed cofacial π-stacking provide a structural basis for the enhanced solid-state fluorescence efficiency observed for **1c** relative to **1b**.

Among this subset, **1d** (torsion ∼21°) provides an interesting contrast to **1a**: despite similar planarity, its excitation spectrum is broad and featureless, lacking the vibronic resolution seen for **1a**, suggesting weaker 0–0 oscillator strength and increased inhomogeneous broadening from lattice disorder. Although both **1b** and **1d** lack strong cofacial π–π stacking interactions, their solid-state packing motifs differ substantially. In compound **1b**, the A-ring is almost perpendicular to the B-ring (Fig. S24, SI), which exhibits a larger A-ring–enone torsional angle and adopts a loosely packed lamellar arrangement. Such packing provides only limited restriction on intramolecular motions, facilitating nonradiative decay and resulting in a low solid-state quantum yield. In contrast, **1d** packs into laterally offset, sheet-like assemblies that restrict intramolecular motion while avoiding close cofacial π–π overlap, resulting in partial rigidification of the chromophore and a higher fluorescence quantum yield than observed for **1b** (Fig. S27, SI). This packing motif partially rigidifies the molecular framework while avoiding strong excitonic coupling, despite its broader excitation features.

The most sterically hindered derivatives, **1e** and **1f**, exhibit the largest A-ring-backbone torsional distortions (∼78° and ∼65°, respectively), which reduce effective conjugation and yield blue-shifted crystalline emission (λ_{em} = 650 and 618 nm). In **1e**, this distortion is coupled with inefficient packing (Fig. S28), producing a broad excitation profile and nearly quenched emission (Φ_{fl} = 0.03). By contrast, **1f**, despite similar torsion, displays the highest crystalline quantum yield of the series (Φ_{fl} = 0.363). Structural analysis (Fig. 9 and Fig. S29) shows that **1f** assembles into donor–acceptor–donor (D–A–D) dimers stabilized by short methoxy-methoxy contacts (∼3.62 Å), with dimers packing orthogonally relative to one another. This geometry rigidifies the chromophore, suppressing torsional and isomerization motions that dominate in

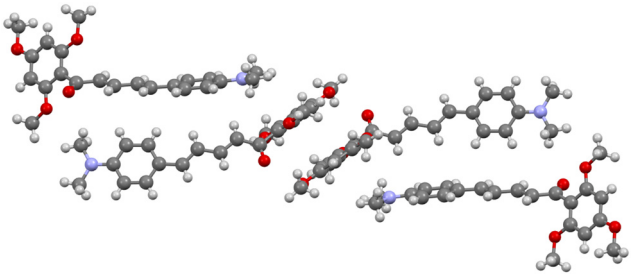

Fig. 9 Crystal packing of **1f** illustrating the D–A–D dimer complex and orthogonal packing of neighbouring molecules.

solution, while simultaneously minimizing exciton migration and self-quenching. Consequently, the excitation profile of **1f** is broad, yet lattice-enforced rigidity channels relaxation into radiative decay, affording the highest solid-state Φ_{fl} in the series.

Computational studies

Time-dependent density functional theory (TDDFT) calculations were performed to compare the theoretical electronic structure with the experimentally observed absorption and emission properties of chalcones **1a–1f**. Ground-state geometries were optimized at the B3LYP/6-311G(d) level using the polarizable continuum model (PCM) in dichloromethane (Fig. S30).

Kohn–Sham HOMO–LUMO gap energies were calculated and span a relatively narrow range of 2.94–3.24 eV across chalcones **1a–1f** (Table S5), consistent with the strong intramolecular charge-transfer (ICT) characteristic.[33–35] The modest variation in KS gap energies indicates that the donor–acceptor framework remains electronically well coupled across the series, and that substituent effects do not substantially alter the intrinsic Frontier orbital energy separation. Instead, these effects primarily influence the spatial distribution and overlap of the Frontier orbitals, which governs the efficiency and extent of charge redistribution upon excitation.

The calculated KS gap values establish a ground-state electronic baseline for comparison of both experimental photophysics and the TDDFT excitation energies. Conversion of the experimental absorption maxima to transition energies ($\sim$2.84–2.99 eV) yields values slightly lower than the corresponding KS gaps, as expected due to excitonic stabilization and orbital relaxation in the excited state (Table S5). The proximity of these energy scales is consistent with efficient donor–acceptor communication and supports assignment of the lowest-energy absorption bands to ICT-dominated transitions. Importantly, because the KS gaps remain comparable across the series, differences in absorption and emission behavior are more reasonably attributed to substituent-induced conformational and orbital redistribution effects rather than large changes in intrinsic electronic coupling.

TDDFT-predicted absorption maxima (λ_{abs}, Table 4) reproduce the experimental trends reasonably well, exhibiting modest red shifts of 9–16 nm for chalcones **1a–1d** and larger deviations of 39–41 nm for the dual *ortho*-methoxy derivatives **1e** and **1f** (Table S5). The larger discrepancies observed for **1e** and **1f** are attributed to the increased steric demand imposed by *ortho*-methoxy substitution, which promotes conformational distortion and attenuated conjugation that are not fully captured at this level of theory.

Table 4 Calculated absorbance and emission values for chalcones **1a–1f** in CH_2Cl_2

Compound	λ_{abs} (nm)	λ_{em} (nm)
1a	446	510
1b	440	501
1c	443	505
1d	435	495
1e	456	516
1f	456	478

In contrast, the calculated emission maxima are systematically blue-shifted relative to experimental values (Table S6). TDDFT-predicted emission energies ($E_{em} \approx$ 2.40–2.60 eV; λ_{em} = 478–516 nm) significantly overestimate the experimentally observed values in DCM ($E_{em} \approx$ 2.12–2.29 eV; λ_{em} = 542–586 nm) by $\sim$0.3–0.6 eV across the series (Table S5). This discrepancy is substantially larger than that observed for absorption energies and reflects extensive excited-state relaxation prior to emission. These results suggest that the fluorescence occurs from a strongly stabilized intramolecular charge-transfer (ICT) minimum that involves pronounced geometric reorganization and charge redistribution in the S_1 state, which is not fully captured by single-reference TDDFT at this level of theory. The magnitude and consistency of the emission energy lowering therefore provide direct evidence for a dominant ICT-driven relaxation pathway in the emissive state, consistent with the large Stokes shifts, pronounced solvatochromism, and low-temperature blue-shifted emission observed experimentally.

Analysis of the optimized ground-state geometries reveals interplanar dihedral angles between the A-ring and the enone backbone ranging from approximately 51 to 63° across the series (Fig. S30). For chalcones **1a–1d**, these moderate torsions preserve sufficient conjugation between donor and acceptor segments to support efficient ICT upon photoexcitation, consistent with their red-shifted emission and higher fluorescence efficiencies. In contrast, the *ortho*-methoxy-substituted derivatives **1e** and **1f** adopt more sterically distorted conformations due to the positioning of the methoxy group, predisposing these molecules toward additional torsional relaxation in the excited state. This enhanced twisting reduces orbital overlap, destabilizes the ICT state, and may promote access to twisted intramolecular charge-transfer (TICT) configurations, rationalizing their hypsochromically shifted emission and reduced quantum yields.

Frontier orbital analyses further support this interpretation. As illustrated in the HOMO–LUMO plots (Fig. 10 and Fig. S30), the HOMOs of all chalcones are primarily localized on the donor and carbonyl moieties, with minimal contribution from the A-ring. The LUMO of **1a** exhibits significant electron density delocalized onto the A-ring, indicating that the ICT process extends beyond the carbonyl unit to incorporate the aryl acceptor fragment. This A-ring participation is progressively

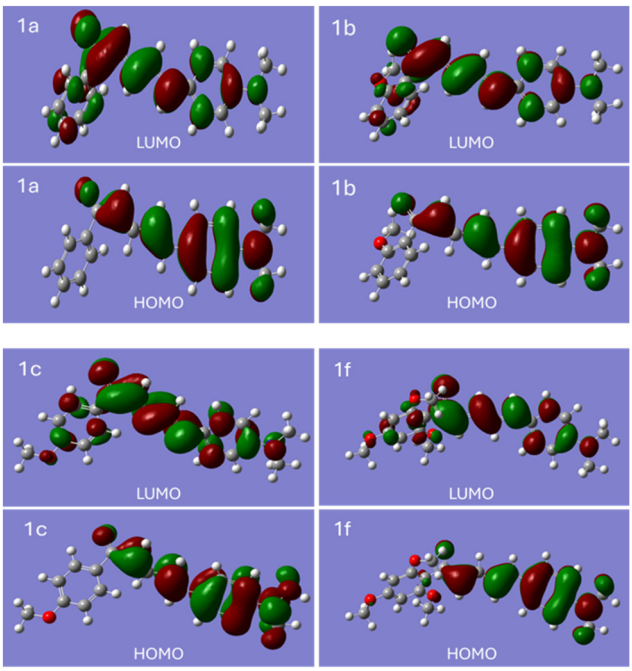

Fig. 10 HOMO–LUMO diagrams of selected chalcones calculated using B3LYP/6-311G(d) in DCM.

diminished in the LUMOs of **1b** and **1c**, consistent with perturbation of ICT by methoxy substitution at the *para* or *ortho* positions. The effect is further amplified in **1e** and **1f**, where steric congestion leads to markedly reduced A-ring contribution in the LUMO, in agreement with the experimentally observed attenuation of ICT and diminished emissive performance.

Conclusion

A series of methoxy-substituted chalcone derivatives with extended π-conjugation were synthesized to examine the structure–property correlation for methoxy-substituted chalcone derivatives. These chalcones exhibit a diene bridge (–CH═CH–CH═CH–) in the center of the molecular backbone, which should increase the probability of *cis–trans* isomerization of vinyl bonds that promote nonradiative decay. Spectroscopic studies showed that these chalcones retained the desirable emission in the red region (λ_{em} ≈ 640–660 nm, Fig. 2), while exhibiting higher fluorescence quantum yields by about 4–8 fold in comparison with **2DHC** (a 2′-hydroxychalcone derivative with the same backbone). In a polar aprotic solvent (*e.g.* DMSO or CH_3CN), some chalcone derivatives exhibited fluorescence quantum yields as high as Φ_{fl} ≈ 0.3, indicating that the presence of a diene bridge is not a limiting factor in developing highly fluorescent materials.

Systematic spectroscopic studies and computational analyses further revealed that emission properties could be governed mainly by the fragments that are in the path of intramolecular charge transfer (ICT). Although the aromatic A-ring is not in the path of ICT, an e-donating group on the A-ring could increase the electron on the C═O group, thereby weakening the ICT and modulating the fluorescence properties. In solution, when the A-ring was *less bulky* (*e.g.* in **1a–1c** with R_1 = H– or CH_3O–, R_3 = H), the ICT was only slightly affected, which has little impact on the fluorescence λ_{em} and Φ_{fl} (Fig. 2 and 4), and lifetime (Table 2). This was further confirmed by using chalcones **1e** and **1f** with a *bulkier* A-ring (with both R_1 and R_3 are CH_3O–). Due to the steric interaction between R_3 and the diene bridge, the D–π–A fragment will no longer adopt a planar conformation desirable for an efficient ICT process. Such steric interaction can lead to emission at a shorter wavelength (Fig. 2) and lower fluorescence Φ_{fl} (Fig. 4). Fluorescence lifetime data of **1e** and **1f** showed that the ICT was no longer the predominant emissive species. The assumption of substitution-assisted perturbation on ICT was also supported by the computational study. The study provides a useful blueprint for controlling the ICT process in chalcones and designing the of next-generation donor–acceptor fluorophores with tailored excited-state behavior.

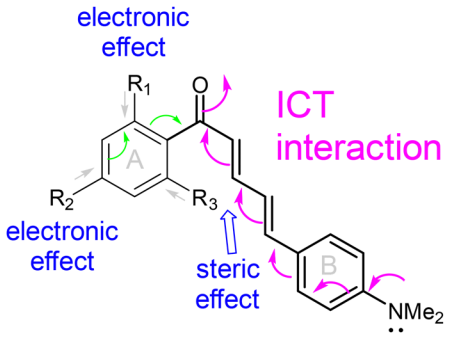

Studies in their solid states provided additional knowledge about these fluorescent materials. Fluorescence studies showed that chalcones **1a–1f** were highly fluorescent in their crystalline solid states, producing red-shifted emission compared to the solution (*e.g.* 703 nm for **1a**). X-ray crystallography of these chalcones revealed their torsional and packing geometry in the solid state. Orthogonally packed donor–acceptor–donor dimers (**1f**) yielded the highest solid-state quantum yield (Φ_{fl} = 0.363), in sharp contrast to its weak Φ_{fl} in solution (Fig. 4). The enhanced fluorescence in the solid could be attributed to the tight packing in a rigid crystal lattice due to the bulky A-ring.

Author contributions

B. C. and Y. P. conceived the study and designed the experiments. B. C. and P. H. synthesized all compounds and performed photophysical studies. W.-Y. C. performed the X-ray crystallographic study under the supervision of C. Z. Finally, B. C. and Y. P. wrote the manuscript with contributions from all co-authors. All authors contributed to the editing of the manuscript.

Conflicts of interest

There are no conflicts to declare.

Data availability

The data supporting this manuscript have been included as part of the supplementary information (SI), including NMR spectra, fluorescence lifetimes and crystal packings.

Supplementary information is available. See DOI: https://doi.org/10.1039/d5ma01288k.

CCDC 2497318–2497323 contain the supplementary crystallographic data for this paper.[36a–f]

Acknowledgements

The study is supported by NIH Grant 1R15GM148965-01 (to Y. P.). We would like to thank Chad Studvick for his help in procuring the computational results.

References

1 M. K. Samota, D. K. Yadav, P. Koli, M. Kaur, M. Kaur, H. Rani, S. S. Selvan, P. Mahala, K. Tripathi and S. Kumar, Exploring Natural Chalcones: Innovative Extraction Techniques, Bioactivities, and Health Potential, *Sustainable Food Technol.*, 2024, **2**, 1456–1468, DOI: 10.1039/d4fb00126e.

2 K. Mezgebe, Y. Melaku and E. Mulugeta, Synthesis and Pharmacological Activities of Chalcone and Its Derivatives Bearing N-Heterocyclic Scaffolds: A Review, *ACS Omega*, 2023, **8**, 19194–19211, DOI: 10.1021/acsomega.3c01035.

3 K. Goyal, R. Kaur, A. Goyal and R. Awasthi, Chalcones: A review on synthesis and pharamacological activities, *J. Appl. Pharm. Sci.*, 2021, **11**, 001–014, DOI: 10.7324/JAPS.2021.11s101.

4 Z. Rozmer and P. Perjési, Naturally Occurring Chalcones and Their Biological Activities. in *Phytochemistry Reviews*, Springer, Netherlands, 2016, pp. 87–120, DOI: 10.1007/s11101-014-9387-8.

5 B. Salehi, C. Quispe, I. Chamkhi, N. El Omari, A. Balahbib, J. Sharifi-Rad, A. Bouyahya, M. Akram, M. Iqbal, A. O. Docea, C. Caruntu, G. Leyva-Gómez, A. Dey, M. Martorell, D. Calina, V. López and F. Les, Pharmacological Properties of Chalcones: A Review of Preclinical Including Molecular Mechanisms and Clinical Evidence, *Front. Pharmacol.*, 2021, **11**, 592654, DOI: 10.3389/fphar.2020.592654.

6 Y. Ouyang, J. Li, X. Chen, X. Fu, S. Sun and Q. Wu, Chalcone Derivatives: Role in Anticancer Therapy, *Biomolecules*, 2021, **11**(6), 894, DOI: 10.3390/biom11060894.

7 N. A. A. Elkanzi, H. Hrichi, R. A. Alolayan, W. Derafa, F. M. Zahou and R. B. Bakr, Synthesis of Chalcones Derivatives and Their Biological Activities: A Review, *ACS Omega*, 2022, 27769–27786, DOI: 10.1021/acsomega.2c01779.

8 K. Mezgebe, Y. Melaku and E. Mulugeta, Synthesis and Pharmacological Activities of Chalcone and Its Derivatives Bearing N-Heterocyclic Scaffolds: A Review, *ACS Omega*, 2023, 19194–19211, DOI: 10.1021/acsomega.3c01035.

9 B. S. Al-Saadi, A. R. Ibrahim, J. Husband, A. H. Ismail, Y. Baqi and O. K. Abou-Zied, Enhanced Intramolecular Charge Transfer and Near-Infrared Fluorescence in 4-Dimethylamino-Chalcone Analogues through Extended Conjugation: Synthesis, Photophysical Properties, and Theoretical Modelling, *Phys. Chem. Chem. Phys.*, 2024, **26**(16), 12844–12851, DOI: 10.1039/d4cp00289j.

10 B. Corbin, P. Houglan and Y. Pang, Fluorescence of 2-Hydroxy Chalcone Analogs with Extended Conjugation: ESIPT vs. ICT Pathways, *Molecules*, 2024, **29**(24), 5972, DOI: 10.3390/molecules29245972.

11 B. Zhou, P. Jiang, J. Lu and C. Xing, Characterization of the Fluorescence Properties of 4-Dialkylaminochalcones and Investigation of the Cytotoxic Mechanism of Chalcones, *Arch. Pharm.*, 2016, 539–552, DOI: 10.1002/ardp.201500434.

12 Z. Luo, T. Lv, K. Zhu, Y. Li, L. Wang, J. J. Gooding, G. Liu and B. Liu, Paper-Based Ratiometric Fluorescence Analytical Devices towards Point-of-Care Testing of Human Serum Albumin, *Angew. Chem., Int. Ed.*, 2020, **59**(8), 3131–3136, DOI: 10.1002/anie.201915046.

13 F. Kamecki, C. Marcucci, M. Ferreira-Gomes, L. Sabatier, D. Knez, S. Gobec, J. L. E. Monti, M. Rademacher, A. Marcos, F. de Tezanos Pinto, L. Gavernet, N. Colettis and M. Marder, 2′-Hydroxy-4′,5′-Dimethyl-4-Dimethylaminochalcone, a Novel Fluorescent Flavonoid with Capacity to Detect Aluminium in Cells and Modulate Alzheimer's Disease Targets, *J. Photochem. Photobiol., A*, 2021, **409**, 113137, DOI: 10.1016/j.jphotochem.2021.113137.

14 M. Ono, R. Watanabe, H. Kawashima, C. Yan, H. Kimura, H. Watanabe, M. Haratake, H. Saji and M. Nakayama, Fluoro-Pegylated Chalcones as Positron Emission Tomography Probes for in Vivo Imaging of β-Amyloid Plaques in Alzheimer's Disease, *J. Med. Chem.*, 2009, **52**(20), 6394–6401, DOI: 10.1021/jm901057p.

15 J. O. Escobedo, O. Rusin, S. Lim and R. M. Strongin, NIR Dyes for Bioimaging Applications, *Curr. Opin. Chem. Biol.*, 2010, 64–70, DOI: 10.1016/j.cbpa.2009.10.022.

16 B. Zhou, P. Jiang, J. Lu and C. Xing, Characterization of the Fluorescence Properties of 4-Dialkylaminochalcones and Investigation of the Cytotoxic Mechanism of Chalcones, *Arch. Pharm.*, 2016, 539–552, DOI: 10.1002/ardp.201500434.

17 Y. Yamakita, N. Yokoyama, B. Xue, N. Shiokawa, Y. Harabuchi, S. Maeda and T. Kobayashi, Femtosecond Electronic Relaxation and Real-Time Vibrational Dynamics in 2′-Hydroxychalcone, *Phys. Chem. Chem. Phys.*, 2019, **21**(10), 5344–5358, DOI: 10.1039/c8cp06405a.

18 M. Dommett and R. Crespo-Otero, Excited State Proton Transfer in 2′-Hydroxychalcone Derivatives, *Phys. Chem. Chem. Phys.*, 2017, **19**(3), 2409–2416, DOI: 10.1039/c6cp07541j.

19 C. S. Abeywickrama, Large Stokes Shift Benzothiazolium Cyanine Dyes with Improved Intramolecular Charge Transfer (ICT) for Cell Imaging Applications, *Chem. Commun.*, 2022, **58**(71), 9855–9869, DOI: 10.1039/d2cc03880c.

20 A. Loudet and K. Burgess, BODIPY Dyes and Their Derivatives: Syntheses and Spectroscopic Properties, *Chem. Rev.*, 2007, 4891–4932, DOI: 10.1021/cr078381n.

21 L. D. Lavis and R. T. Raines, Bright Ideas for Chemical Biology, *ACS Chem. Biol.*, 2008, 142–155, DOI: 10.1021/cb700248m.

22 L. Yuan, W. Lin, K. Zheng, L. He and W. Huang, Far-Red to near Infrared Analyte-Responsive Fluorescent Probes Based on Organic Fluorophore Platforms for Fluorescence Imaging, *Chem. Soc. Rev.*, 2013, **42**(2), 622–661, DOI: 10.1039/c2cs35313j.

23 Z. R. Grabowski, K. Rotkiewicz and W. Rettig, Structural Changes Accompanying Intramolecular Electron Transfer: Focus on Twisted Intramolecular Charge-Transfer States and Structures, *Chem. Rev.*, 2003, 3899–4031, DOI: 10.1021/cr940745l.

24 H. Chen, B. Dong, Y. Tang and W. Lin, A Unique ''Integration'' Strategy for the Rational Design of Optically Tunable Near-Infrared Fluorophores, *Acc. Chem. Res.*, 2017, **50**(6), 1410–1422, DOI: 10.1021/acs.accounts.7b00087.

25 A. Bhattacharyya, S. C. Makhal and N. Guchhait, Comparative Photophysical Study of Differently Substituted Cinnamaldehyde-Based Chalcones: From Intramolecular Charge Transfer to Fluorogenic Solvent Selectivity, *J. Phys. Chem. A*, 2019, **123**(30), 6411–6419, DOI: 10.1021/acs.jpca.9b03437.

26 B. S. Al-Saadi, A. R. Ibrahim, J. Husband, A. H. Ismail, Y. Baqi and O. K. Abou-Zied, Enhanced Intramolecular Charge Transfer and Near-Infrared Fluorescence in 4-Dimethylamino-Chalcone Analogues through Extended Conjugation: Synthesis, Photophysical Properties, and Theoretical Modelling, *Phys. Chem. Chem. Phys.*, 2024, **26**(16), 12844–12851, DOI: 10.1039/d4cp00289j.

27 S. Sasaki, G. P. C. Drummen and G. I. Konishi, Recent Advances in Twisted Intramolecular Charge Transfer (TICT) Fluorescence and Related Phenomena in Materials Chemistry, *J. Mater. Chem. C*, 2016, 2731–2743, DOI: 10.1039/c5tc03933a.

28 D. J. Stewart, M. J. Dalton, S. L. Long, R. Kannan, Z. Yu, T. M. Cooper, J. E. Haley and L. S. Tan, Steric Hindrance Inhibits Excited-State Relaxation and Lowers the Extent of Intramolecular Charge Transfer in Two-Photon Absorbing Dyes, *Phys. Chem. Chem. Phys.*, 2016, **18**(7), 5587–5596, DOI: 10.1039/c5cp07716h.

29 C. Chen and C. Fang, Fluorescence Modulation by Amines: Mechanistic Insights into Twisted Intramolecular Charge Transfer (TICT) and Beyond, *Chemosensors*, 2023, **11**(2), 87, DOI: 10.3390/chemosensors11020087.

30 S. Sasaki, Y. Niko, A. S. Klymchenko and G. I. Konishi, Design of Donor-Acceptor Geometry for Tuning Excited-State Polarization: Fluorescence Solvatochromism of Push-Pull Biphenyls with Various Torsional Restrictions on Their Aryl-Aryl Bonds, *Tetrahedron*, 2014, **70**(41), 7551–7559, DOI: 10.1016/j.tet.2014.08.002.

31 M. Pietrzak, M. Józefowicz, A. Bajorek and J. R. Heldt, Experimental and Theoretical Studies of the Spectroscopic Properties of Chalcone Derivatives, *J. Fluoresc.*, 2017, **27**(2), 537–549, DOI: 10.1007/s10895-016-1981-2.

32 B. S. Al-Saadi, A. R. Ibrahim, J. Husband, A. H. Ismail, Y. Baqi and O. K. Abou-Zied, Enhanced Intramolecular Charge Transfer and Near-Infrared Fluorescence in 4-Dimethylamino-Chalcone Analogues through Extended Conjugation: Synthesis, Photophysical Properties, and Theoretical Modelling, *Phys. Chem. Chem. Phys.*, 2024, **26**(16), 12844–12851, DOI: 10.1039/d4cp00289j.

33 E. J. Baerends, From the Kohn-Sham Band Gap to the Fundamental Gap in Solids. An Integer Electron Approach, *Phys. Chem. Chem. Phys.*, 2017, 15639–15656, DOI: 10.1039/c7cp02123b.

34 J. Jia, S. Wu, Y. Lu, J. Xu, H. Zuo, X. Wu and Y. Song, Controlling Stimulated Emission via Intramolecular Charge Transfer in Amino-Coumarin Dyes: Switching from Reverse Saturable to Saturable Absorption, *Molecules*, 2025, **30**(18), 3799, DOI: 10.3390/molecules30183799.

35 A. K. Narsaria, J. Poater, C. Fonseca Guerra, A. W. Ehlers, K. Lammertsma and F. M. Bickelhaupt, Rational Design of Near-Infrared Absorbing Organic Dyes: Controlling the HOMO–LUMO Gap Using Quantitative Molecular Orbital Theory, *J. Comput. Chem.*, 2018, **39**(32), 2690–2696, DOI: 10.1002/jcc.25731.

36 (*a*) CCDC 2497318: Experimental Crystal Structure Determination, 2026, DOI: 10.5517/ccdc.csd.cc2ptnnv; (*b*) CCDC 2497319: Experimental Crystal Structure Determination, 2026, DOI: 10.5517/ccdc.csd.cc2ptnpw; (*c*) CCDC 2497320: Experimental Crystal Structure Determination, 2026, DOI: 10.5517/ccdc.csd.cc2ptnqx; (*d*) CCDC 2497321: Experimental Crystal Structure Determination, 2026, DOI: 10.5517/ccdc.csd.cc2ptnry; (*e*) CCDC 2497322: Experimental Crystal Structure Determination, 2026, DOI: 10.5517/ccdc.csd.cc2ptnsz; (*f*) CCDC 2497323: Experimental Crystal Structure Determination, 2026, DOI: 10.5517/ccdc.csd.cc2ptnt0.